PCCP

ROYAL SOCIETY OF CHEMISTRY

PAPER

View Article Online
View Journal | View Issue

Cite this: *Phys. Chem. Chem. Phys.*, 2020, **22**, 15488

Two dimensional ruthenium carbide: structural and electronic features

T. Gorkan,[a] S. Demirci,[bc] S. Jahangirov,[c] G. Gökoğlu[d] and E. Aktürk[*ae]

Received 12th April 2020,
Accepted 4th June 2020

DOI: 10.1039/d0cp01990a

rsc.li/pccp

The design and realization of novel 2D materials and their functionalities have been a focus of research inspired by the successful synthesis of graphene and many other 2D materials. In this study, in view of first principles calculations, we predict a novel 2D material ruthenium carbide (RuC) in graphene-like honeycomb hexagonal lattice with planar geometry. Phonon dispersion spectra display a dynamically stable structure. Comprehensive molecular dynamics calculations confirm the stability of the structure up to high temperatures as ≈1000 K. The system is a narrow gap semiconductor with a band gap of 53 meV (345 meV) due to GGA-PBE (HSE) calculations. Band gap exhibits significant changes by applied strain. Elastic and optical properties of the system are examined in monolayer form. RuC/RuC bilayer, RuC/graphene and RuC/h-BN heterostructures are also investigated. By calculating the phonon dispersion it is verified that RuC bilayer is the most stable in AA type-stacking configuration where Ru and C atoms of both layers have identical lateral coordinates. The effects of atomic substitutions on electronic band structures, acting as p-type and n-type doping, are revealed. A novel 3D RuCLi structure is also predicted to be stable and the isolation of its monolayer forms are discussed. Ruthenium carbide, as a 2D material which is dynamically and thermally stable, holds promise for applications in nanoelectronics.

1 Introduction

Two-dimensional (2D) nanomaterials have been attracting a huge deal of attention,[1] since the experimental synthesis of graphene from graphite by mechanical cleavage method,[2] *i.e.* graphene is a single-atom-thick sheet of carbon atoms arranged in a hexagonal lattice constructing a honeycomb pattern. Although graphene is described as an ideal 2D material, the ripples in graphene due to thermal fluctuations at any finite temperature make it 3D in nature.[3,4] Graphene displays various distinct properties like ultra-high electron mobility at room temperature,[2] high Young's modulus (≈1 TPa),[5] and extraordinary thermal conductivity (3000–5000 W m^{-1} K^{-1}).[6] Unprecedented properties of graphene have turned attentions to other elements of group IV, *e.g.* silicon, germanium and tin. It was reported that silicon, germanium and tin can be stabilized in 2D buckled-honeycomb lattices, namely, silicene, germanene, stanene, respectively. sp^3 hybridization in silicene, germanene and stanene results in buckled geometry as a different case from graphene which is sp^2 hybridized carbon atoms arranged in a planar lattice.[7–10] Among these systems, stanene has topologically nontrivial states which are tunable and can be changed from π to σ orbitals through functionalization.[9] Various group III–IV and group II–VI compounds have also been predicted theoretically and observed to be stable at room temperature.[7,11–18] SiC and h-BN (hexagonal BN) monolayer structures have also planar geometry similar to graphene.[13] h-BN system, also referred to as white graphene due to its optically transparent nature, is a representative 2D material with wide band gap ≈6 eV and can be a complementary dielectric substrate for graphene based applications.[19]

Since graphene is a semi-metal with zero electronic density of states at Fermi level (E_F), its gapless nature greatly limits the applications in optoelectronics. Transition metal dichalcogenides (TMDs) with an ultra-thin layered structure, particularly MoS_2, is a demanding materials for developing two-dimensional nano-electronic devices with an intrinsic direct band gap which can easily be tuned.[20–27] Various TMD systems have been shown to be stable with diverse electronic ground states, *e.g.* semiconducting, half-metallic, and metallic.[28] Group III monochalcogenides in the form of MX (M = Ga, In and X = S, Se, Te), *e.g.* GaS, have been successfully fabricated to be used in photodetector applications.[29] Single crystalline 2D GaSe is also a p-type semiconductor with high photoresponsivity (≈1.7 A W^{-1} under white light illumination).[30]

[a] *Department of Physics, Adnan Menderes University, 09100 Aydın, Turkey. E-mail: ethem.akturk@adu.edu.tr; Fax: +90 2562135379; Tel: +90 2562130835*
[b] *Department of Physics, Kırıkkale University, 71450 Kırıkkale, Turkey*
[c] *UNAM-Institute of Materials Science and Nanotechnology, Bilkent University, 06800 Ankara, Turkey*
[d] *Department of Mechatronics Engineering, Faculty of Engineering, Karabuk University, 78050 Karabuk, Turkey*
[e] *Nanotechnology Application and Research Center, Adnan Menderes University, 09100 Aydn, Turkey*

The successful synthesis of 2D counterpart of layered black phosphorus, *i.e.* phosphorene, has brought the monolayers of group-V elements into attention.[31–34] Phosphorene is a p-type semiconductor with sp^3 hybridized phosphorus atoms forming a puckered geometry. Moreover, 2D monolayer structures of arsenic (arsenene),[35–37] antimony (antimonene),[38,39] and bismuth (bismuthene)[40,41] have also been predicted theoretically.

Transition metal carbides have been attracting great interest due to their high chemical and thermal stability with potential applications in capacitors and batteries.[42,43] Naguib *et al.* have reported the synthesis of 2D transition metal carbides and cabonitrides, namely MXenes, from MAX phases in which A layer is removed by selective etching.[44] Li *et al.* have shown that niobium carbide MXenes are promising supports for nanoparticle catalysts.[45] Recent advances in synthesis and biomedical applications of MXenes have been comprehensively reviewed by Huang *et al.*[46] Ultrathin Mo_2C crystals have been obtained by chemical vapour deposition method and shown to be superconducting.[47]

In this study, we explore a novel 2D transition metal carbide structure, ruthenium carbide (RuC), in view of density functional calculations. We observe that RuC forms a graphene-like hexagonal honeycomb structure with planar geometry which is highly preserved up to elevated temperatures, 1000 K. Electronic, optical, and elastic behaviors are revealed. RuC bilayer is investigated with different stacking configurations. Electronic natures of RuC/graphene and RuC/h-BN heterostructures are studied. We also give the electronic modifications of RuC by substituting one carbon atom with B (p-type) and N (n-type) atoms. Major findings of the present study can be summarized as follows: (i) RuC monolayer is stable up to temperatures far above room temperature. (ii) The system is a semiconductor with a narrow energy band gap which can easily be tuned by applied strain and elemental doping. (iii) Monolayer RuC exhibits an in-plane stiffness of $\approx$69 J m^{-2} which is larger than that of silicene. (iv) RuC monolayer can also be stabilized on graphene and h-BN sheets. (v) 3D RuCLi layered bulk structure is both energetically and dynamically stable. It can also be possible to isolate $RuCLi_2$ monolayer from this bulk phase.

2 Computational details

All the first principles calculations presented in this work are based on the spin-polarized density functional theory (DFT) using plane-wave basis sets. Spin–orbit coupling (SOC) effect is also included in calculations. Projector augmented wave (PAW)[48] potentials are used to describe electron–ion interactions as implemented in the Vienna ab initio simulation package (VASP).[49] Generalized gradient approximation (GGA) with Perdew–Burke–Ernzerhof (PBE)[50] parametrization is used to mimic exchange–correlation interactions including van der Waals (vdW) correction. The kinetic energy cutoff value for the expansion of plane-waves is set to 650 eV. The *k*-point mesh of 15 × 15 × 1 are used for monolayer systems. *k*-Mesh and cut-off energy values are tested for the convergence of the total energy. We employ following supercells for monolayer, bilayer, and heterostructure systems: the 3 × 3 supercell for RuC, 4 × 4 for graphene and h-BN structures. The electronic and geometric relaxation of the structures are performed using supercell geometry with a vacuum distance about 15 Å in perpendicular direction to monolayer surface, which is large enough to avoid interactions between two adjacent monolayers in the periodic arrangement. Atomic positions are optimized using the conjugate gradient (CG) method, where all the atomic coordinates are fully relaxed until the Hellman–Feynman force on each atom is less than 0.001 eV $Å^{-1}$. The energy convergence criterion of the electronic self-consistency was taken as 10^{-5} eV between two successive iterations. Gaussian type Fermi-level smearing method is used with a smearing width 0.01 eV. We calculate the average cohesive energy to reveal the energetic stability of the system at zero temperature and zero pressure. The average cohesive energy (per atom) of a monolayer including *n* Ru and *m* C atoms is calculated as:

$$E_c = (nE_{Ru} + mE_C - E_{RuC})/(n + m) \quad (1)$$

where E_{RuC} is the calculated total energy of monolayer RuC, E_{Ru} and E_C are the calculated total energies of isolated Ru and C atoms, respectively. $E_c > 0$ indicates that the formation of free standing monolayer is favorable relative to free constituent atoms. Hence the higher E_c the stronger is the cohesion.

Ab initio phonon dispersion spectra are obtained using real space force constants of the supercell within the framework of DFPT as implemented in the VASP code combined with PHONOPY package[51] using an energy convergence criterion of 10^{-8} eV. Phonon calculation have been performed using a 4 × 4 × 1 supercell and 3 × 3 × 1 grid for *k*-point. All MD calculations have been performed using a 3 × 3 × 1 supercell and 5 × 5 × 1 *k*-point grid. A Nosé thermostat was used, and Newton's equation of motion were integrated through the Verlet algorithm with time steps of 2 fs.

Defining A_0 as the equilibrium area of the system, the in-plane stiffness constant is given as:[52]

$$C = \frac{1}{A_0}\frac{\partial^2 E_s}{\partial \varepsilon^2} \quad (2)$$

where E_s is the strain energy calculated by subtracting the total energy of the strained system from the equilibrium total energy and ε is the uniaxial strain ($\varepsilon = \Delta a/a$, a being the lattice constant).

Poisson's ratio which is the ratio of transverse strain to the axial strain can be defined as:[52]

$$\nu = -\frac{\varepsilon_{trans}}{\varepsilon_{axial}} \quad (3)$$

3 Results and discussion

Here, we report and discuss 2D ruthenium monocarbide monolayer and its structural analogous systems in a wide perspective. This section is organized as follows: firstly, we present the structural search details and the method for choosing the system investigated. We present the structural stability and comprehensive physical properties of monolayer RuC (ML-RuC) in the second subsection.

The properties of RuC bilayer, RuC/graphene and RuC/h-BN heterostructures are displayed in third subsection. Finally, we introduce a novel bulk 3D RuCLi system and the stability of its corresponding monolayer structures are discussed.

3.1 Structure search and stability of the system proposed

We have performed a comprehensive structural search by CALYPSO code which provides an efficient way to discover the stable structure with minimum enthalpy for a given atomic composition by generating a large number of random configurations.[53–55] CALYPSO also utilizes several techniques for global structural minimization from scratch.[54] Particle Swarm Optimization technique was successfully applied to several systems with various chemical-bonding environments.[54] We first performed a search for possible structures in a 2-atom cell containing 1 Ru and 1 C atoms. We performed two sets of calculations with 1 Å and 2 Å initial buckling. As a result, the 2D structure with lowest enthalpy has a honeycomb lattice conforming to $P\bar{6}m2$ (#187) space group whereby atoms are distributed in the same plane just like graphene. As shown below, this structure is dynamically stable. We also performed another search with 2 Ru and 2 C atoms. The lowest enthalpy 2D structure found in this search is a buckled structure. This structure has a square lattice and conforms to $P4/nmm$ space group. The square structure has $\sim$0.5 eV higher cohesive energy compared to the honeycomb structure. However, the square lattice RuC system is not dynamically stable with various imaginary phonon branches along the high symmetry directions of the Brillouin zone.

Furthermore, bulk structures with lower energy including $F\bar{4}3m$ (#216) and $P\bar{6}m2$ (#187) space groups are also proposed as a result of the CALYPSO calculations. Hexagonal ($P\bar{6}m2$, #187) and face-centered cubic ($F\bar{4}3m$, #216) bulk structures have $\sim$0.5 and 0.7 eV lower energy than 2D honeycomb structure, respectively. These results are consistent with previous knowledge, since Zhao *et al.* have reported that cubic zinc blende RuC is the most stable 3D structure energetically among 10 structures of known transition-metal compounds.[56] In view of these results, we focus on the hexagonal honeycomb monolayer structure of RuC (ML-RuC) with planar geometry.

3.2 Structure, electronic, elastic, and optical properties of ML-RuC

We first obtain the optimized structure of 2D RuC monolayer in graphene-like honeycomb lattice. Top and side views of the equilibrium ground state structure with planar geometry is given in Fig. 1a. Our calculated Ru–C bond length is 1.88 Å which is shorter than the Ru–C bond length of zinc blende (zb) RuC which is $\approx$1.97 Å as reported previously in view of first principles calculations.[56] It should be noted that zb-RuC is the most stable phase of bulk structure of RuC which is a semiconducting superhard material with high bond strength, while other crystallographic phases, *e.g.* hexagonal and cubic, are mostly metallic. Generally, a shorter bond length means a stronger bond for a pair of given atoms. The calculated cohesive energy per atom of ML-RuC is 6.98 eV per atom, while cohesive energy of bulk zinc blende RuC is 7.99 eV per atom. That means our monolayer RuC system is energetically favorable relative to free Ru and C atoms, but the stability is lower than the most stable bulk phase.

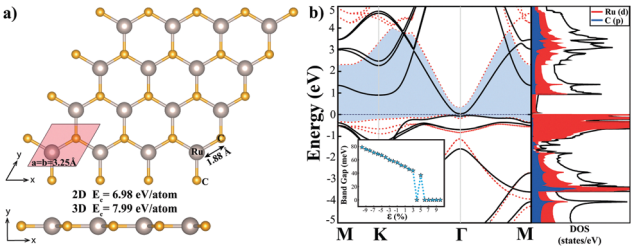

Fig. 1 (a) Top and side views of optimized atomic structure of ML-RuC. (b) Electronic band structure (HSE dotted lines) and orbital projected density of electronic states of ML-RuC. The variation of band gap under strain is also given as an inset.

We have checked the dynamical stability of the structure by calculating phonon dispersion spectra as given in Fig. 2a. Phonon dispersion consists of 6 well defined vibrational branches and displays no vibrational anomaly along any direction of the Brillouin zone indicating a dynamically stable structure. Out-of-plane transverse acoustic mode (ZA) or flexural mode has lowest frequency range compared to other acoustic modes indicating a quadratic dispersion near Γ-point similar to graphene. We also apply equilibrium constant temperature molecular dynamics simulations to investigate thermal stability at room and elevated temperatures. In Fig. 2b, we display the *ab initio* molecular dynamics results in which the structure is kept at temperatures 300 K, 500 K, and 1000 K for 2 ps. It is seen that the structural robustness of the system is maintained without any thermal decomposition even at 1000 K, although the planar form of ML-RuC is slightly modified due to thermal fluctuations.

Electronic energy band structure and electronic density of states of ML-RuC are given in Fig. 1b. ML-RuC is a narrow direct gap semiconductor with a band gap of 53 meV due to PBE-GGA calculations. HSE06 hybrid functional calculations result in a improved band gap of 345 meV at Γ-point. Energy gap is largely restricted by Ru-d states. Bonding states are composed of Ru-d and C-p orbitals. The strong hybridization between these d–p orbitals results in high bond strength. In Fig. 1b, the variation of band gap is shown as a function of applied strain as an inset of band structure. We see that band gap can be opened by applied tensile (negative) strain, while compressive (positive) strain displays metallization of the system with vanishing band gap. Due to GGA-PBE calculations, band gap can be increased up to $\approx$80 meV by a strain of 10%.

It is known that the inclusion of impurities in semiconducting crystals largely modifies the electrical conductivity. In Fig. 3, we give electronic band structures and atom projected electronic density of states of impurity-doped systems. A carbon atom is replaced by boron (or nitrogen) atom acting as acceptor (or donor) states. B-Doped system is still a semiconductor with 5 meV indirect band gap along Γ–K points. Band gap is determined by Ru states similar to bare ML-RuC, while B-p states are located below Fermi level around -2 eV. On the other hand, N-doped ML-RuC is a metal with Ru bands crossing

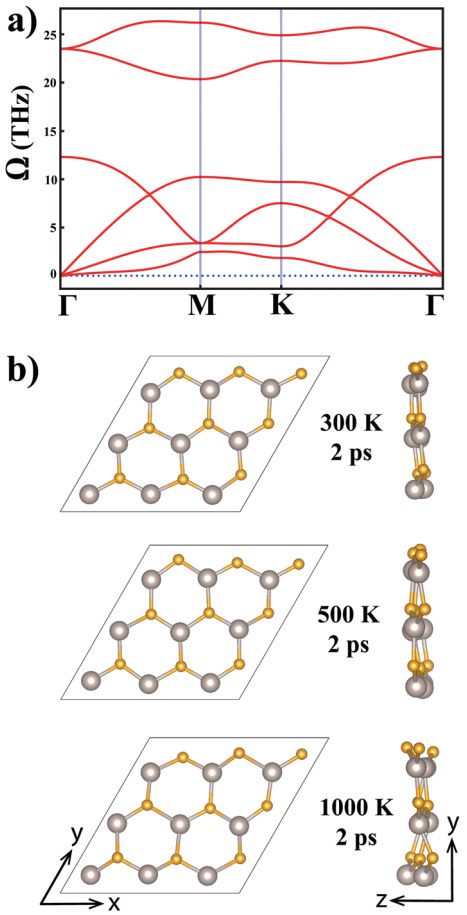

Fig. 2 (a) *Ab initio* phonon dispersion curves of ML-RuC. (b) Equilibrium constant temperature molecular dynamics simulation results of ML-RuC at 300, 500 and 1000 K.

Fermi level. These results indicate that electronic nature of ML-RuC can be tuned by elemental doping as well as applied strain.

We give 3D plot of total energy as a function of lattice constant in Fig. 4 which reflects the qualitative view of mechanical response of the material to applied biaxial strain. Stretching and bending behavior of 2D materials are important for growth on suitable substrates. It is seen that energy stored by the system increases rapidly if the system is compressed or elongated in both directions in the material plane where we use a rectangular cell for related calculations. We observe that the system has almost isotropic in-plane stiffness of $\approx$69 J m^{-2} (C_x = 69.34 J m^{-2} and C_y = 69.26 J m^{-2}) which is close to that of silicene.[57] Poisson's ratio, which is also isotropic, is 0.73 which value is close to that of black phosphorene.[58] It can be said that ML-RuC system has promising elastic properties which are comparable to known 2D materials like silicene and black phosphorene. Additionally, these elastic parameters are suitable for design and actuation of devices. In a previous work, elastic stiffness tensor components of phosphorene were reported between 18.4 and 105.2 GPa nm which reflects a highly anisotropic nature.[58] Another study presents a comprehensive investigation on 2D carbides MXenes.[59] That work reports 135 and 214 N m^{-1} in-plane elastic stiffness for Ti_2C and Ti_3C_2, respectively. It is also diplayed that $Nb_4C_3T_2$ (T = O, OH, F)

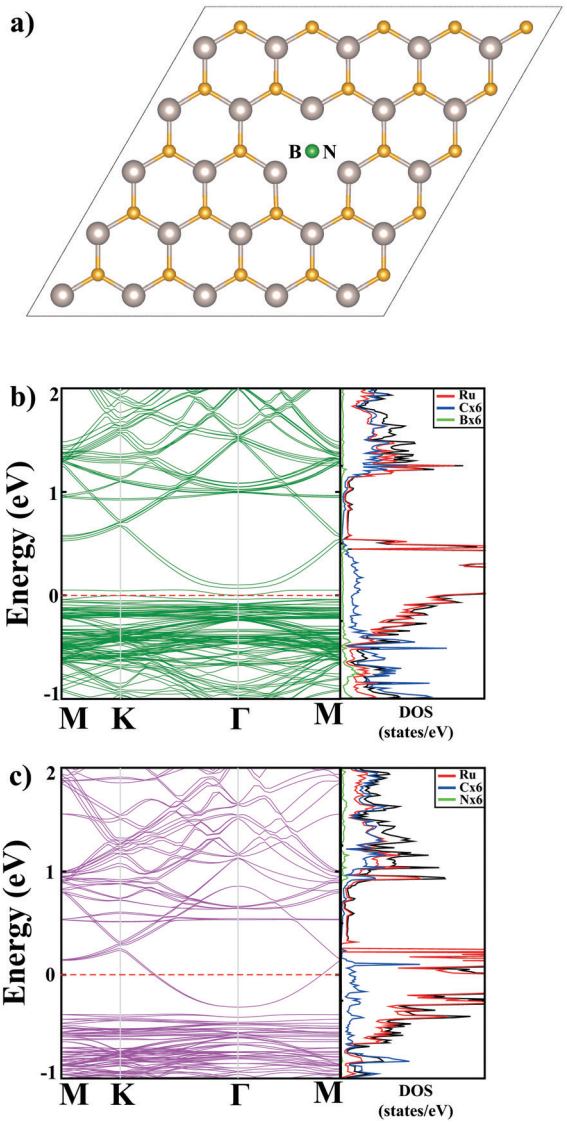

Fig. 3 (a) B- or N-atom doped structure. Electronic band structure and site projected density of electronic states of (b) B-doped and (c) N-doped monolayer system. Density of states of B, C, and N atoms are multiplied by six to become comparable with that of Ru atom.

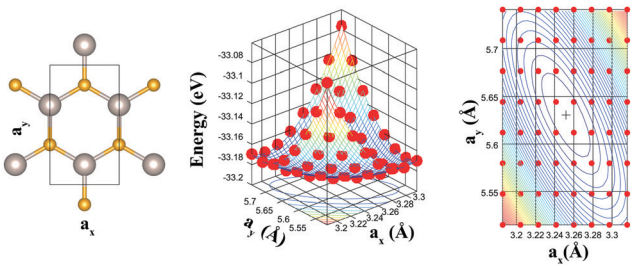

Fig. 4 Three dimensional view of lattice constants and corresponding total energy values of ML-RuC. The projections on *xy*-plane are also given as a contour plot. Equilibrium state with minimum energy is indicated by + sign in contours.

MXene systems exhibit a stiffness up to 600 N m^{-1}. Elastic properties of 2D $Ti_3C_2T_x$ (T_x: F, O, OH) MXene monolayers and

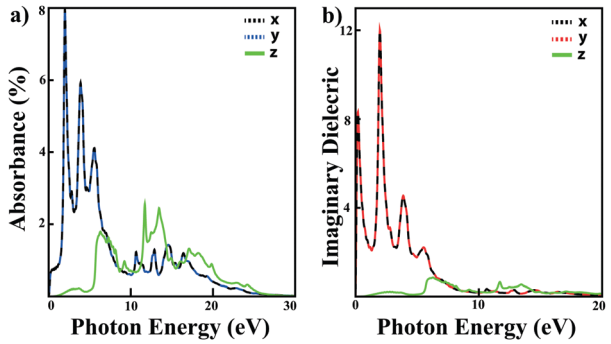

Fig. 5 (a) Absorbance and (b) imaginary dielectric function as a function of photon energy for ML-RuC.

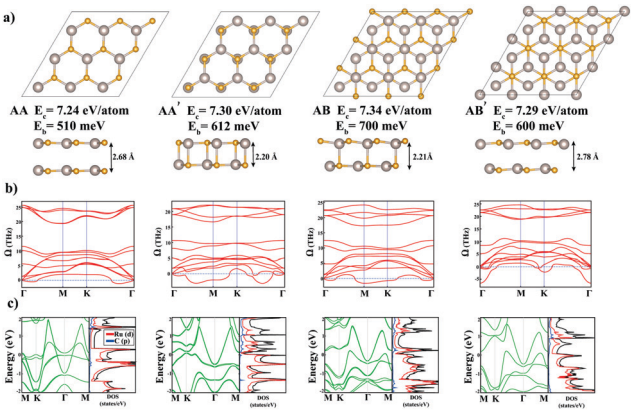

Fig. 6 (a) Top and side views of RuC bilayer at four different stacking configurations. (b) *Ab initio* phonon dispersion curves and (c) electronic band structures and orbital projected density of electronic states of RuC bilayer systems.

bilayers were investigated experimentally.[60] They report that $Ti_3C_2T_x$ flakes have 326 ± 29 N m^{-1} average 2D elastic modulus. In a recent first principles study, in-plane elastic stiffness of a series of TiMC (M: Zr, Hf, Cr, Mo) systems are given between 102.9 and 151.9 N m^{-1}.[61] It is seen that the stiffness of MXene systems covers a wide range due to diversity of the constituent atoms. As a comparison, other well-known 2D materials like graphene (338 N m^{-1}), MoS_2 (123 N m^{-1}), and h-BN (267 N m^{-1}) have relatively larger stiffness values.[59] However, ML-RuC system, as presented in this work, is a one-atom-thick crystal as a different case from other MXene systems which have a layered structure.

The absorbance is an optical parameter which is a measure of the intensity attenuation of an incident electromagnetic wave, while the imaginary part of the complex dielectric function shows the interband transitions of a semiconducting material. These parameters are shown in Fig. 5 as a function of photon energy. The optical response of the material is almost same in *x*- and *y*-directions (in-plane directions), while the behavior in *z*-direction is rather different. Along *x*- and *y*-directions, the absorption starts at low energies due to very low band gap. Absorbance shows remarkable peaks between 0–6 eV energy range where incident photons are absorbed by the material resulting the excitation of an electron to conduction band. This is also consistent with the imaginary dielectric function where the peaks are observed at approximately same energy values. The absorbance of high energy photons between 10–20 eV energy range is also possible with lower probability. The material has a notable absorbance in the perpendicular-to-plane direction between 10–15 eV.

3.3 Bilayer RuC and heterostructures

Beyond the free standing ML-RuC, we construct bilayer RuC, RuC/graphene and RuC/h-BN heterostructures to investigate the stability of ML-RuC on specific nanosheet supports. In Fig. 6a, we present the RuC bilayer structures considered at four different stacking configurations. All the structures have cohesive energies between 7.24–7.34 eV per atom which are larger than that of ML-RuC, that means bilayers have increased stability compared to ML-RuC in any stacking configuration. As shown in Fig. 6a, we calculate the binding energies of RuC bilayer systems at four stacking configurations as 510–700 meV which shows that bilayer structures are more favorable than single layer RuC sheet indicating a remarkable binding. This significant interaction is also revealed by short interlayer distance between RuC monolayers which has a maximum value of 2.78 Å for AB′ stacking. Aierken *et al.* have calculated binding energies of various MXene bilayer systems (M_2CX_2 where M = Sc, Ti, V and X = OH, O) around ≈20 meV per atom.[62] In a recent study of Li *et al.*, binding energies of asymmetric MXene/transition metal dichalcogenide systems were reported as 0.49–1.36 eV per cell following a similar computational methodology.[63] In another study,[64] binding energies per unit cell of MX_2/MoS_2 heterobilayers were given between 0.14 and 0.31 eV. We also display the electronic band structures and partial density of electronic states of bilayer RuC in Fig. 6c. It is observed that narrow gap semiconducting character of ML-RuC is altered to yield a metallic behavior in bilayers at all stacking configurations. The electronic ground states of the bilayer systems are largely controlled by Ru-d orbitals which cover the states around Fermi level similar to ML-RuC. These Ru-d states around E_F are due to hybridizations between Ru-d orbitals of individual monolayers. In the ground state, six Ru-d electrons occupy d_{xy}, d_{xz} and d_{yz} states. These d-electrons can be excited to d_{z^2} and $d_{x^2-y^2}$ states to form a bilayer structure with remarkable bonding between the individual monolayers.

Besides the energetic stability, we also study the dynamic stability of RuC bilayers by calculating phonon dispersion spectra as shown in Fig. 6b. Although all the structures have energetic stability, phonon dispersion spectra consist of imaginary and anomalous vibrational modes. Due to vibrational spectra, AA-type stacking seems to be more stable dynamically with negative frequencies which are close to *Γ*-point. In this context, it can be said that particular acoustic branches at long wavelength limit ($\lambda \gg a$, $k \to 0$) can exhibit vibrational anomaly for AA-stacked bilayer.

ML-RuC have similar structural motif with graphene and h-BN with different electronic nature. We show the optimized RuC/graphene and RuC/h-BN vertical heterostructures and their electronic bands in Fig. 7. ML-RuC is stabilized at 3.16 and 2.85 Å distances above graphene and h-BN sheets, respectively. As a comparison, graphene/h-BN heterostructure has ≈3.1 Å

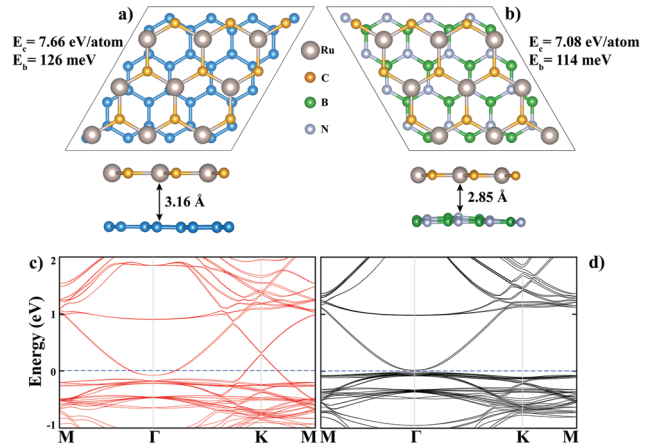

Fig. 7 (a) Top and side views of graphene/RuC heterostructure and (c) its electronic bands. (b) Top and side views of h-BN/RuC heterostructure and (d) its electronic bands.

vertical distance as a typical van der Waals heterostructure system.[65] In-plane B–N and C–C bond lengths are calculated as 1.43 and 1.42 Å in RuC/h-BN and RuC/graphene heterostructures, respectively. These values reveal a relatively high lattice mismatch of ≈24% between RuC and h-BN or graphene sheets, since Ru–C bond length is 1.88 Å as mentioned previously. However, we do not observe a structural deformation in planar form of related 2D monolayers as seen in Fig. 7. As a different case from strongly bonded heterointerfaces, van der Waals (vdW) heterostructures of 2D materials with weak interactions, *e.g.*, graphene, boron nitride and transition metal dichalcogenides, can be realised by epitaxial growth techniques.[66–69] It was shown that novel heterostructures with outstanding properties can be realized despite of large lattice mismatch and unfavorable crystal lattice orientations,[66,67] so that the design and functionalisation of novel nanodevices can also be feasible in the existence of structural constraints.

Binding energy of ML-RuC on graphene or h-BN surfaces can be calculated by: $E_b = (E_{RuC} + E_{graph.} - E_{RuC/graph.})/N$ where E_{RuC} and $E_{graph.}$ are the total energies of RuC and graphene monolayers, respectively, while $E_{RuC/graph.}$ is the energy of heterostructure and N is total number of atoms in ML-RuC. We find 126 and 114 meV binding energy per atom for RuC/graphene and RuC/h-BN systems, respectively. Our calculated values are consistent with the literature, since van der Waals bonds in typical heterostructures have binding energy between 0.1–0.3 eV.[64] Yelgel reports that binding energy of buckled stanene on graphene-like nitrides changes between 79 and 314 meV per Sn atom.[70] Electronic character of pristine ML-RuC is largely altered by realization of heterostructures as seen in Fig. 7c and d. Graphene/RuC system is metallic with Ru-d bands crossing Fermi level around *K*- and *Γ*-points. However, h-BN/RuC system is still semiconductor with 32 meV direct band gap at *K*-point. It is seen that ML-RuC system can be coupled to other monolayer structures yielding a modified electronic character.

3.4 Bulk 3D RuCLi and its analogous 2D structures

In addition to ML-RuC and its structural and electronic modifications, we also predict a novel 3D RuCLi structure with rhombohedral symmetry and its monolayer forms. In Fig. 8a, we present the bulk RuCLi structure which conforms to D_{3d} point group with lattice constant of $a = b = c = 3.46$ Å. This structure is similar to hexagonal monolayer RuC as discussed above with Li layers between RuC honeycomb planes yielding a metallic system. The planar form of ML-RuC is slightly destroyed upon optimization and becomes buckled. In this structure, Ru–C bond length increases to 2.12 Å which is larger than that of pristine ML-RuC. Cohesive energy of the system is 6.23 eV per atom indicating an energetically favorable structure. In order to check dynamical stability, we also obtain *ab initio* phonon dispersion curves of 3D RuCLi. As seen in Fig. 8a, the system is dynamically stable without any vibrational anomaly and softening of phonon modes along any symmetry directions in irreducible Brillouin zone.

We also investigate whether a monolayer structure can be isolated from 3D RuCLi. In Fig. 8b and c, we give the RuCLi and $RuCLi_2$ monolayers which consist of ML-RuC with Li atoms covering one or two sides. In this context, these monolayers can be formed by bombarding ML-RuC with Li atoms at one or two sides experimentally. The structural parameters of RuCLi and $RuCLi_2$ monolayers are similar with cohesive energies of 5.71 and 4.98 eV per atom, respectively. Phonon spectra of both systems contain a negative acoustic mode indicating dynamical instability. But, it can be concluded that $RuCLi_2$ monolayer system is more stable dynamically, so it has an imaginary vibrational mode around *Γ*-point. Moreover, this imaginary mode is out-of-plane acoustical vibrational branch. From the

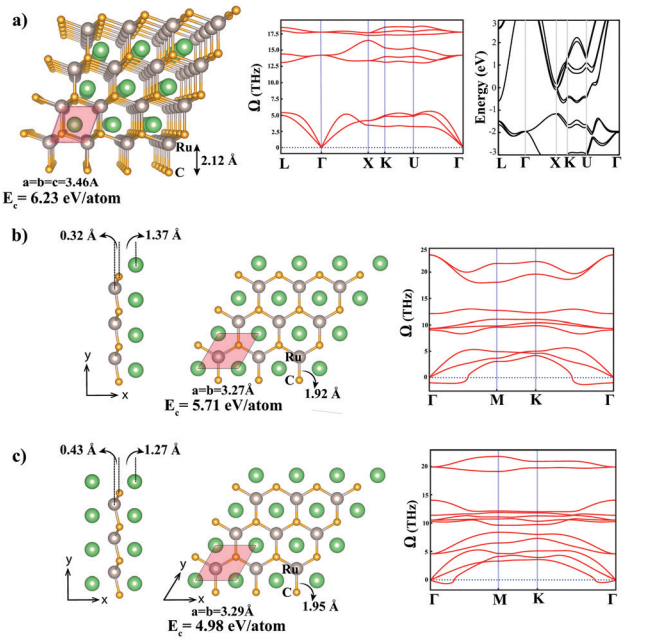

Fig. 8 (a) 3D bulk structure of RuCLi in rhombohedral symmetry with *ab initio* phonon dispersion curves and electronic bands. (b) RuCLi and (c) $RuCLi_2$ monolayer structures and their *ab initio* phonon dispersion curves.

technological point of view, we calculate the theoretical lithium storage capacity of $RuCLi_2$ monolayer as 421 mA h g^{-1}, so that it can be used as a promising energy storage material for various applications.

4 Conclusion

We have introduced a novel 2D material RuC monolayer system in graphene-like honeycomb lattice which is energetically, dynamically and thermally stable. The system is a narrow gap semiconductor. The electronic band gap of the system can be tuned by applied strain. The doping of ML-RuC with trivalent (boron) or pentavalent (nitrogen) atoms can also alter the electronic nature of the system. RuC monolayer has promising elastic behavior with an in-plane elastic stiffness constant comparable to buckled silicene. RuC bilayer, graphene/RuC, and h-BN/RuC structures are also energetically favorable. We discover a novel 3D structure RuCLi which is composed of Li-intercalated RuC monolayers. This system is also stable both energetically and dynamically. We suggest that $RuCLi_2$ monolayer can be constructed by covering both sides of ML-RuC with Li atoms. This monolayer system can be seen as a promising lithium storage material.

Conflicts of interest

There are no conflicts to declare.

Acknowledgements

Computing resources used in this work were provided by the TUBITAK ULAKBIM, High Performance and Grid Computing Center (Tr-Grid e-Infrastructure). This work was supported by the Research Fund of the Adnan Menderes University under Project No. FEF-17012. S. D. thanks UNAM, National Nanotechnology Research Center at Bilkent University for the hospitality. S. J. acknowledges support from the Turkish Academy of Sciences – Outstanding Young Scientists Award Program (TÜBA-GEBIP).

References

1 H. Zhang, *ACS Nano*, 2015, **9**, 9451–9469.
2 K. S. Novoselov, A. Geim, S. Morozov, D. Jiang, Y. Zhang, S. Dubonos, I. Grigorieva and A. A. Firsov, *Science*, 2004, **306**, 666–669.
3 D. Geng and H. Y. Yang, *Adv. Mater.*, 2018, **30**, 1800865.
4 A. K. Singh and R. G. Hennig, *Phys. Rev. B: Condens. Matter Mater. Phys.*, 2013, **87**, 094112.
5 C. Lee, X. D. Wei, J. W. Kysar and J. Hone, *Science*, 2008, **321**, 385–388.
6 A. A. Balandin, S. Ghosh, W. Bao, I. Calizo, D. Teweldebrhan, F. Miao and C. N. Lau, *Nano Lett.*, 2008, **8**, 902–907.
7 E. Durgun, S. Tongay and S. Ciraci, *Phys. Rev. B: Condens. Matter Mater. Phys.*, 2005, **72**, 075420.
8 S. Cahangirov, M. Topsakal, E. Akturk, H. Sahin and S. Ciraci, *Phys. Rev. Lett.*, 2009, **102**, 236804.
9 J. Deng, B. Xia, X. Ma, H. Chen, H. Shan, X. Zhai, B. Li, A. Zhao, Y. Xu, W. Duan, S.-C. Zhang, B. Wang and J. G. Hou, *Nat. Mater.*, 2018, **17**, 1081–1086.
10 P. Vogt, P. DePadova, C. Quaresima, J. Avila, E. Frantzeskakis, M. C. Asensio, A. Resta, B. Ealet and G. L. S. Lay, *Phys. Rev. Lett.*, 2012, **108**, 155501.
11 T. Gorkan, E. Aktürk and S. Ciraci, *Phys. Rev. B: Condens. Matter Mater. Phys.*, 2019, **100**, 125306.
12 K. S. Novoselov, D. Jiang, F. Schedin, T. J. Booth, V. V. Khotkevich, S. V. Morozov and A. K. Geim, *Proc. Natl. Acad. Sci. U. S. A.*, 2005, **102**, 10451–10453.
13 H. Sahin, S. Cahangirov, M. Topsakal, E. Bekaroglu, E. Akturk, R. T. Senger and S. Ciraci, *Phys. Rev. B: Condens. Matter Mater. Phys.*, 2009, **80**, 155453.
14 M. Topsakal, E. Akturk and S. Ciraci, *Phys. Rev. B: Condens. Matter Mater. Phys.*, 2009, **79**, 115442.
15 E. Bekaroglu, M. Topsakal, S. Cahangirov and S. Ciraci, *Phys. Rev. B: Condens. Matter Mater. Phys.*, 2010, **81**, 075433.
16 M. Topsakal, S. Cahangirov, E. Bekaroglu and S. Ciraci, *Phys. Rev. B: Condens. Matter Mater. Phys.*, 2009, **80**, 235119.
17 V. O. Ozcelik, E. Durgun and S. Ciraci, *J. Phys. Chem. Lett.*, 2014, **5**, 2694–2699.
18 D. Kecik, A. Onen, M. Konuk, E. Gurbuz, F. Ersan, S. Cahangirov, E. Akturk, E. Durgun and S. Ciraci, *Appl. Phys. Rev.*, 2018, **5**, 011105.
19 L. Song, L. Ci, H. Lu, P. B. Sorokin, C. Jin, J. Ni, A. G. Kvashnin, D. G. Kvashnin, J. Lou, B. I. Yakobson and P. M. Ajayan, *J. Phys. Chem. C*, 2010, **10**, 3209–3215.
20 K. F. Mak, C. Lee, J. Hone, J. Shan and T. F. Heinz, *Phys. Rev. Lett.*, 2010, **105**, 136805.
21 B. Radisavljevic, A. Radenovic, J. Brivio, V. Giacometti and A. Kis, *Nat. Nanotechnol.*, 2011, **6**, 147–150.
22 M. Chhowalla, H. S. Shin, G. Eda, L. L. Li, K. P. Loh and H. Zhang, *Nat. Chem.*, 2013, **5**, 263–275.
23 L. Rapoport, Yu. Bilik, Y. Feldman, M. Homyonfer, S. R. Cohen and R. Tenne, *Nature*, 1997, **387**, 791–793.
24 C. Ataca, H. Sahin, E. Akturk and S. Ciraci, *J. Phys. Chem. C*, 2011, **115**, 3934–3941.
25 C. Ataca, M. Topsakal, E. Akturk and S. Ciraci, *J. Phys. Chem. C*, 2011, **115**, 16354–16361.
26 H. G. Füchtbauer, A. K. Tuxen, P. G. Moses, H. Topsøe, H. Besenbacher and J. V. Lauritsen, *Phys. Chem. Chem. Phys.*, 2013, **15**, 15971–15980.
27 M. Javaid, D. W. Drumm, S. P. Russo and A. D. Greentree, *Sci. Rep.*, 2017, **7**, 9775.
28 C. Ataca, H. Sahin and S. Ciraci, *J. Phys. Chem. C*, 2012, **116**, 8983–8999.
29 S. Yang, Y. Li, X. Wang, N. Huo, J.-B. Xia, S.-S. Li and J. Li, *Nanoscale*, 2014, **6**, 2582–2587.
30 X. Li, M.-W. Lin, A. A. Puretzky, J. C. Idrobo, C. Ma, M. Chi, M. Yoon, C. M. Rouleau, I. I. Kravchenko, D. B. Geohegan and K. Xiao, *Sci. Rep.*, 2014, **4**, 5497.

31 L. Li, Y. Yu, G. J. Ye, Q. Ge, X. Ou, H. Wu, D. Feng, X. H. Chen and Y. Zhang, *Nat. Nanotechnol.*, 2014, **9**, 372–377.
32 Y. Zhang, N. Dong, H. Tao, C. Yan, J. Huang, T. Liu, A. W. Robertson, J. Texter, J. Wang and Z. Sun, *Chem. Mater.*, 2017, **29**, 6445–6456.
33 F. Ersan, D. Kecik, V. O. Ozcelik, Y. Kadioglu, O. Akturk Uzengi, E. Durgun, E. Akturk and S. Ciraci, *Appl. Phys. Rev.*, 2019, **6**, 021308.
34 H. Liu, A. T. Neal, Z. Zhu, Z. Luo, X. Xu, D. Tomanek and P. D. Ye, *ACS Nano*, 2014, **8**, 4033–4041.
35 C. Kamal and M. Ezawa, *Phys. Rev. B: Condens. Matter Mater. Phys.*, 2015, **91**, 085423.
36 D. Kecik, E. Durgun and S. Ciraci, *Phys. Rev. B*, 2016, **94**, 205409.
37 D. Kecik, E. Durgun and S. Ciraci, *Phys. Rev. B*, 2016, **94**, 205410.
38 O. Akturk Uzengi, V. O. Ozcelik and S. Ciraci, *Phys. Rev. B: Condens. Matter Mater. Phys.*, 2015, **91**, 235446.
39 Z. Zhang, Z. Yan, Y. Li, Z. Chen and H. Zeng, *Angew. Chem., Int. Ed.*, 2015, **54**, 3112–3115.
40 E. Akturk, O. Akturk Uzengi and S. Ciraci, *Phys. Rev. B*, 2016, **94**, 014115.
41 F. Ersan, E. Akturk and S. Ciraci, *Phys. Rev. B*, 2016, **94**, 245417.
42 Y. Xiao, J.-Y. Hwang and Y.-K. Sun, *J. Mater. Chem. A*, 2016, **4**, 10379–10393.
43 Y. Gogotsi, *Nat. Mater.*, 2015, **14**, 1079–1080.
44 M. Naguib, O. Mashtalir, J. Carle, V. Presser, J. Lu, L. Hultman, Y. Gogotsi and M. W. Barsoum, *ACS Nano*, 2012, **6**, 1322–1331.
45 Z. Li, Y. Cui, Z. Wu, C. Milligan, L. Zhou, G. Mitchell, B. Xu, E. Shi, J. T. Miller, F. H. Ribeiro and Y. Wu, *Nat. Catal.*, 2018, **1**, 349–355.
46 K. Huang, Z. Li, J. Lin, G. Han and P. Huang, *Chem. Soc. Rev.*, 2018, **47**, 5109.
47 C. Xu, L. Wang, Z. Liu, L. Chen, J. Guo, N. Kang, X.-L. Ma, H.-M. Cheng and W. Ren, *Nat. Mater.*, 2015, **14**, 1135.
48 P. E. Blöchl, *Phys. Rev. B: Condens. Matter Mater. Phys.*, 1994, **50**, 17953.
49 G. Kresse and J. Furthmuller, *Phys. Rev. B: Condens. Matter Mater. Phys.*, 1996, **54**, 11169.
50 J. P. Perdew, K. Burke and M. Ernzerhof, *Phys. Rev. Lett.*, 1996, **77**, 3865.
51 A. Togo and I. Tanaka, *Scr. Mater.*, 2015, **108**, 1–5.
52 M. Topsakal, S. Cahangirov and S. Ciraci, *Appl. Phys. Lett.*, 2010, **96**, 091912.
53 Y. Wang, J. Lv, L. Zhu and Y. Ma, *Comput. Phys. Commun.*, 2012, **183**, 2063–2070.
54 Y. Wang, J. Lv, L. Zhu and Y. Ma, *Phys. Rev. B: Condens. Matter Mater. Phys.*, 2010, **82**, 094116.
55 B. Gao, P. Gao, S. Lu, J. Lv, Y. Wang and Y. Ma, *Sci. Bull.*, 2019, **64**, 301.
56 Z. Zhao, M. Wang, L. Cui, J. He, D. Yu and Y. Tian, *J. Phys. Chem. C*, 2010, **114**, 9961–9964.
57 Q. Peng, X. Wen and S. De, *RSC Adv.*, 2013, **3**, 13772–13781.
58 L. Wang, A. Kutana, X. Zou and B. I. Yakobson, *Nanoscale*, 2015, **7**, 9746–9751.
59 T. Hu, J. Yang, W. Li, X. Wang and C. Ming-Li, *Phys. Chem. Chem. Phys.*, 2020, **22**, 2115–2121.
60 A. Lipatov, H. Lu, M. Alhabeb, B. Anasori, A. Gruverman, Y. Gogotsi and A. Sinitskii, *Sci. Adv.*, 2018, **4**, eaat0491.
61 Y. Hu, X. L. Fan, W. J. Guo, Y. R. An, Z. F. Luo and J. Kong, *J. Magn. Magn. Mater.*, 2018, **486**, 165280.
62 Y. Aierken, C. Sevik, O. Gülseren, F. M. Peeters and D. Cakir, *J. Mater. Chem. A*, 2018, **6**, 2337–2345.
63 B. Li, H. Guo, Y. Wang, W. Zhang, Q. Zhang, L. Chen, X. Fan, W. Zhang, Y. Li and W.-M. Lau, *Npj Comput. Mater.*, 2019, **5**, 16.
64 N. Lu, H. Guo, L. Li, J. Dai, L. Wang, W.-N. Mei, X. Wu and X. C. Zeng, *Nanoscale*, 2014, **6**, 2879.
65 J. Yin, J. Li, Y. Hang, J. Yu, G. Tai, X. Li, Z. Zhang and W. Guo, *Small*, 2016, **12**, 2942–2968.
66 A. Ghasemi, D. Kepaptsoglou, P. L. Galindo, Q. M. Ramasse, T. Hesjedal and V. K. Lazarov, *NPG Asia Mater.*, 2017, **9**, 402.
67 A. Koma, *Thin Solid Films*, 1992, **216**, 72–76.
68 K. S. Novoselov, A. Mishchenko, A. Carvalho and A. H. Castro Neto, *Science*, 2016, **353**, 461–472.
69 A. K. Geim and I. V. Grigorieva, *Nature*, 2013, **499**, 419–425.
70 C. Yelgel, *J. Appl. Phys.*, 2019, **125**, 155301.